AJNR

Assessment of Metastatic Cervical Adenopathy Using Dynamic Contrast-Enhanced MR Imaging

Nancy J. Fischbein, Susan M. Noworolski, Roland G. Henry, Michael J. Kaplan, William P. Dillon and Sarah J. Nelson

AJNR Am J Neuroradiol 2003, 24 (3) 301-311
http://www.ajnr.org/content/24/3/301

Assessment of Metastatic Cervical Adenopathy Using Dynamic Contrast-Enhanced MR Imaging

Nancy J. Fischbein, Susan M. Noworolski, Roland G. Henry, Michael J. Kaplan, William P. Dillon, and Sarah J. Nelson

BACKGROUND AND PURPOSE: **Morphologic assessment by conventional imaging methods of lymph node metastases in patients with squamous cell carcinoma of the head and neck is, at best, insensitive. Doppler sonography has shown that lymph node metastases exhibit alterations in the number of vessels and blood flow. We assessed the ability of dynamic contrast-enhanced MR imaging to differentiate normal from diseased nodes in this patient population.**

METHODS: **Twenty-one patients with newly diagnosed squamous cell carcinoma and no previous treatment were studied with the use of a head and neck phased array surface coil. Anatomic imaging included high resolution T1-weighted, fat-saturated fast spin-echo T2-weighted, and contrast-enhanced T1-weighted imaging (0.99–1.32 mm^3 voxels). The dynamic contrast-enhanced MR imaging was performed by using a 2D fast spoiled gradient recalled sequence with single dose bolus injection of contrast agent. Calculated values included time to peak, peak enhancement, maximum slope, and washout slope for the enhancement. All patients underwent neck dissection as part of their indicated treatment, and imaging results were correlated with pathologic findings.**

RESULTS: **Dynamic contrast-enhanced MR imaging and pathology comparisons were obtained for 68 nodes. There was significantly longer time to peak ($P < .001$), lower peak enhancement ($P < .05$), lower maximum slope ($P < .01$), and slower washout slope ($P < .05$) in the tumor-involved nodes compared with the normal nodes.**

CONCLUSION: **Analysis of dynamic contrast-enhanced MR imaging can differentiate normal from diseased lymph nodes in patients with squamous cell carcinoma of the head and neck.**

The status of the cervical lymph nodes is one of the most important factors influencing therapeutic management and outcome for patients with squamous cell carcinoma of the upper aerodigestive tract. Clinical palpation has an accuracy, at best, of approximately 70% (1–3). CT and MR imaging provide additional information regarding nodes that are inaccessible to palpation and may also show nodal necrosis, which is equated with tumor involvement in the appropriate clinical setting (4–6). These modalities can detect metastatic nodes in 38% to 67% of patients with no obvious nodal disease revealed by clinical palpation (7), but both are insensitive to the presence of nonnecrotic tumor within normal sized lymph nodes. When only nodal size is considered (4, 5, 8), a trade-off between sensitivity and specificity is necessary. Metabolic imaging with ^{18}F-flouorodeoxyglucose positron emission tomography (9) and MR imaging with superparamagnetic iron oxide particles (10) offer alternative but not widely available windows into nodal physiology. Sonography-based methods (color Doppler ultrasonography and ultrasonography-guided fine needle aspiration) have been used to assess intranodal angioarchitecture and to provide direct tissue assessment for the presence of metastases (11–13), but these methods also have limitations and are not widely used in this country for screening evaluations.

Dynamic contrast-enhanced MR imaging is a method that allows imaging of the physiology of the microcirculation, which is altered in tumors as compared with normal tissues. This methodology has been applied to the study of tumors of the brain, breast, uterine cervix, bone, bladder, and prostate

Received April 25, 2002; accepted after revision October 8.

Supported by the National Cancer Institute (UO1 CA62561 and KO1 CA76998) and the University of California Cancer Research Coordinating Committee (251510536240).

Presented in part at the American Society of Neuroradiology, San Diego, CA, 1999, and in part at the International Society of Magnetic Resonance in Medicine, Denver, CO, 2000.

From the Departments of Radiology (N.J.F., R.G.H., S.M.N., W.P.D., S.J.N.) and Otolaryngology-Head and Neck Surgery (M.J.K.), University of California, San Francisco, San Francisco, CA.

Address reprint requests to Nancy J. Fischbein, MD, Department of Radiology, University of California, San Francisco, Box 0628, Room L-358, 505 Parnassus Avenue, San Francisco, CA 94143.

TABLE 1: Patient demographic information

Patient No.	Age (y) /Sex	Diagnosis	Preoperative Staging*	Nodal Status on Conventional Images (CT Scan or MR Image)	Postoperative Staging
1	44/F	SCC tongue	T3N1	CT: negative (N1 based on palpation)	T3N2c
2	59/M	SCC floor of mouth	T2N0	MR: negative	T2N0
3	56/M	SCC buccal mucosa	T2N0	MR: negative	T1N0
4	64/F	SCC oropharynx	T3N0	CT:negative	T2N0
5	53/M	SCC oropharynx	T3N2a	MR: multiple abnormal nodes	T3N2a
6	57/M	SCC oropharynx	T4N2c	MR: multiple abnormal nodes	T4N2c
7	52/M	SCC tongue	TxN2b†	MR: multiple abnormal nodes	TxN2b
8	72/M	SCC retromolar trigone	T2N2b	MR: multiple abnormal nodes	T1N2b
9	72/F	SCC nasal cavity	TxN1†	CT: single necrotic node	TxN1
10	63/M	SCC tongue	T3N0	MR: negative	T2N0
11	71/M	SCC tongue	T3N0	MR: negative (but N1 based on PET)	T3N1‡
12	79/F	SCC alveolar ridge	T3N2b	MR: multiple abnormal nodes	T4N2b
13	74/M	SCC retromolar trigone	T2N0	MR: negative	T2N1‡
14	65/F	SCC alveolar ridge	T4N0	MR: negative	T4N0
15	47/M	SCC tongue	TxN2b†	CT: multiple abnormal nodes	TxN2b
16	83/F	SCC tongue	T1N0	MR: negative	T1N0
17	52/M	SCC tongue	T1N0	MR: negative	T1N0
18	44/F	SCC tongue	T1N0	MR: negative	T1N0
19	66/M	SCC alveolar ridge	T4N0	MR: negative	T4N0
20	85/F	SCC buccal mucosa	T4N0	CT: negative	T4N1‡
21	62/M	SCC floor of mouth	TxN2b†	CT: multiple abnormal nodes	TxN2b

Note.—F indicates female; M, male; SCC, squamous cell carcinoma; PET, positron emission tomography.

* All patients were staged as M0. Preoperative staging was based on clinical palpation and conventional anatomic imaging with CT and/or MR imaging, not high resolution MR imaging.

† Primary site previously excised (hence, the "Tx" designation), but no radiation or other therapy to the neck previously received. Patient evaluated and treated for neck disease.

‡ Three patients preoperatively staged as N0 were upstaged to N1 based on pathologic findings.

(14–24). Dynamic contrast-enhanced MR imaging has also been applied to primary cancers of the head and neck (25–31). We performed high resolution surface coil anatomic imaging and dynamic contrast-enhanced MR imaging on a group of patients with squamous cell carcinoma of the head and neck who were undergoing clinically indicated neck dissection to determine whether dynamic contrast-enhanced MR imaging could be used to distinguish tumor-involved from non-tumor-involved lymph nodes.

Methods

Twenty-seven patients with newly diagnosed squamous cell carcinoma of the head and neck whose clinical management included up-front neck dissection (ie, neck dissection before any radiation or chemotherapy) were prospectively identified at our institution's weekly meeting of the Head and Neck Tumor Board. No patient had undergone previous radiation or chemotherapy. All patients underwent MR imaging with the use of a 1.5-T magnet after obtaining informed consent by using a protocol approved by our Institutional Review Board. Each patient had a 22-gauge IV line placed before entering the imaging unit. Imaging was performed by using a custom-built receive-only head and neck phased array surface coil (32). Axial view T1-weighted (600/20/2 [TR/TE/number of excitations]; field of view, 18 cm; matrix, 256 × 192; section thickness, 2 mm; section gap, 1 mm) and fast spin-echo T2-weighted fat-saturated (4000/90/4; field of view, 18 cm; matrix, 256 × 256; section thickness, 2 mm; section gap, 1 mm) images were obtained before the administration of contrast agent. A dynamic 2D fast spoiled gradient recalled sequence (10.4/2.3; flip angle, 30 degrees; field of view, 18 cm; matrix, 256 × 128; section thickness, 4 mm; section gap, 1 mm) was then obtained with 40 time points for 10 locations at a speed of 1.3 s/image during bolus injection (2.5 mL/s) of single dose contrast agent. These parameters limited our superior-to-inferior coverage to 5 cm, and we positioned the sections to cover the main nodal drainage pathways as dictated by the location of the primary tumor (33). Axial view T1-weighted contrast-enhanced fat-saturated images were then obtained (600/20/2; field of view, 18 cm; matrix, 256 × 192; section thickness, 2 mm; section gap, 1 mm). The routine anatomic images were photographed, while the dynamic data were processed off-line on a Sun SPARC workstation.

Six patients were excluded from this analysis. Reasons for exclusion were final pathologic diagnosis was not squamous cell carcinoma, even though that had been suggested at initial fine needle aspiration (n = 2, Hodgkin disease and dendritic cell sarcoma); a variant protocol had been used for the dynamic acquisition (n = 1); and the MR imaging system functioned improperly during acquisition of dynamic data during the early phase of the study (n = 3).

Twenty-one patients therefore formed the study group; the demographic information is presented in Table 1. The anatomic images were reviewed by a head and neck radiologist. Definite lymph nodes (ie, clearly not small blood vessels) were identified and circled, and a prediction was made regarding whether tumor was present based on size (>10 mm in short axis dimension), heterogeneity of signal intensity, or presence of frank necrosis on contrast-enhanced T1-weighted images. Necrosis was defined as areas of low signal intensity on T1-weighted images, high signal intensity on T2-weighted images, and lack of enhancement on contrast-enhanced images. Heterogeneity was defined as irregular areas of abnormally high or low signal intensity on T2-weighted images and/or areas of irregular enhancement but not meeting the criteria for clear-cut necrosis. The review was conducted by a single experienced

observer, and the predictions were charted and recorded. The images were then reviewed in conjunction with the head and neck surgeon. The identified lymph nodes that the surgeon was confident he could individually and specifically identify and dissect within in a reasonable length of time so as not to unduly prolong the patient's time in the operating room were assigned unique identifying labels, and a chart was constructed with the node label and a description of its anatomic localization. This was available in the operating room, as were the high resolution images, and was used to guide operative localization and labeling of specimens for pathologic evaluation. The individually dissected nodes were placed in cassettes labeled with their unique identifier and sent for processing, along with the remainder of the neck dissection specimen. Individual nodes were sliced at 1-mm intervals, routinely processed, and assessed for the presence or absence of tumor foci. The individual nodal labeling was maintained throughout specimen processing. Once the final pathology report was available, this information was correlated with the results of the anatomic and dynamic imaging.

On the Sun SPARC workstation, the images were first corrected for surface coil intensity inhomogeneity by using an edge-completed low pass filter technique (34). Next, they were masked, retaining mostly vessels and nodes, and then the difference between a given section and the reference section was minimized over an 11-point translation right/left and anterior/posterior. The shifts corresponding to the minimum difference between the images were then applied to the original dynamic data. Nodes were localized by using the high resolution fast spin-echo T2-weighted images for guidance, and regions of interest were manually drawn on the nodes on the dynamic images by using software developed in our laboratory, written in the IDL environment (Research Systems, Inc., Boulder, CO).

The regions of interest were drawn by an experienced postdoctoral researcher, guided by a head and neck radiologist. Regions of interest were also drawn on the submandibular gland and the sternocleidomastoid muscle for normalization. To reduce motion artifacts, the dynamic images were automatically aligned in plane. A region of interest was drawn just inside the peripheral margin of the node (not right to the edge because subtle motion of the edges due to pulsation and respiration could result in inclusion of non-nodal tissue in the region of interest), and the region of interest was copied onto the image obtained at each time point through the dynamic acquisition. Individual images were then reviewed, and regions of interest were manually relocated if patient motion (physiological or gross) had caused the region of interest to shift beyond the lymph node boundary. In six cases, individual data points had to be excluded because of brief gross patient movement that could not be corrected by manually relocating the region of interest. In all cases, the region of interest was drawn to encompass the entire node, without specific exclusion of areas of heterogeneity or necrosis, because we wanted to assess the ability of the simplest analysis to detect differences between tumor-involved and non-tumor-involved nodes. In addition, many of our abnormal nodes were heterogeneous but not frankly necrotic, and only four of 68 nodes that had clear-cut areas of gross focal necrosis could be clearly segregated into separate regions of interest. We did, however, perform a subanalysis of the grossly necrotic nodes to assess the effect of studying the rim alone versus the rim plus the necrotic core. Mean signal intensity versus time curves were generated for the region of interest. Peak time (in seconds), peak enhancement (% baseline), and maximum 2-point slope, normalized to baseline intensity and to a 1-min interval, were calculated. Also, a washout slope estimate was calculated from the 5-min late point versus the peak point. This slope was also normalized to baseline intensity/min. Results for the tumor-involved lymph nodes were compared with those for the non-tumor-involved lymph nodes by using *t* tests. For comparisons with the normal tissues, a Student-Neuman-Keuls statistical test was conducted.

Results

Nodal Status

Twelve of 21 patients had their necks preoperatively staged as N0 based on clinical examination and conventional anatomic imaging (CT or MR imaging). In three (25%) of the 12 patients, occult tumor-involved nodes were identified pathologically, consistent with reported false-negative rates for clinical staging in the 15% to 25% range. The condition of one of the 12 had been staged as N1 based on preoperative ^{18}F-flouorodeoxyglucose positron emission tomography, but palpation and conventional anatomic imaging results were normal. The remaining nine patients had evidence of pathologic lymphadenopathy based on clinical or routine imaging criteria, and tumor-involved nodes were found in all cases. Overall, 129 nodes in 21 patients were specifically dissected and presented for pathologic analysis. Of these 129 nodes, 28 were tumor-involved and 101 were non-tumor-involved nodes. Non-tumor-involved nodes could not be further segregated into normal and reactive categories because only the presence or absence of tumor was described pathologically.

Anatomic Imaging

All 129 nodes were assessed for size, heterogeneity of signal intensity, and presence of frank necrosis on thin section high resolution anatomic images. Nodes ranged in size (short axis diameter) from 2 to 25 mm, with a mean of 7.1 mm. Non-tumor-involved nodes ranged in size from 2 to 10 mm (mean, 5.5 mm), and tumor-involved nodes ranged in size from 7 to 25 mm (mean, 12.7 mm; $P < .001$). One hundred two nodes appeared normal, 23 showed areas of heterogeneity (Fig 1), and four showed clearly defined areas of necrosis. The heterogeneity often manifested as irregular areas of low signal intensity on T2-weighted images and less intense enhancement on the contrast-enhanced images, an appearance that may be due to keratin pools in keratinizing squamous cell carcinomas (35). In most cases (124 of 129 cases), imaging and pathologic diagnoses were concordant. Results were discrepant for five nodes, with MR imaging predicting tumor when the node was pathologically normal in two of five cases (questioned subtle heterogeneity in 9- and 7-mm nodes) and MR imaging missing tumor when the node was pathologically abnormal in three of five cases (7-, 8-, and 10-mm nodes). Two of these latter nodes resulted in a patient's condition being upstaged from N0 to N1, as shown in Table 1. All patients underwent routine CT or MR imaging before their high resolution study. In no case did routine CT or MR imaging identify a tumor-involved node that was not seen on high resolution images. A direct node-to-node comparison between conventional and high resolution imaging could not be conducted, however, because differences in image quality, patient positioning, section thickness, and image angulation made definitive correlation difficult for many smaller nodes.

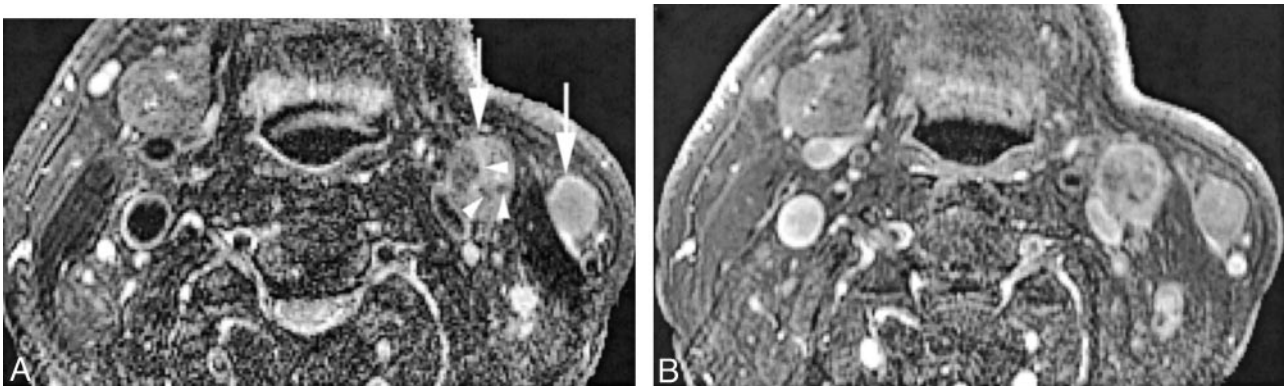

FIG 1. Patient 21, a 62-year-old man who was previously treated for squamous cell carcinoma of the floor of the mouth with primary and level I lymph node resection at an outside institution.

A, Coil-corrected axial view fast spin-echo T2-weighted image with fat saturation (4000/90/4) shows pathologically enlarged left neck nodes in level IIA and superficial to the sternocleidomastoid muscle (*white arrows*). The level IIA node shows internal areas of irregular low signal intensity (*arrowheads*), an appearance we would describe as nodal heterogeneity but not nodal necrosis. Note that it would be impossible to exclude these small, irregular areas from region of interest analysis. Also note the soft tissue deformity and absence of the ipsilateral submandibular gland due to previous resection.

B, Coil-corrected axial view contrast-enhanced T1-weighted image with fat saturation (600/20/2), obtained at the same level as that shown in *A*, shows slightly irregular enhancement of both nodes, with the irregularity clearly more pronounced in the level IIA node. Both nodes were pathologically confirmed to be tumor-involved.

Dynamic Contrast-enhanced Imaging

Dynamic contrast-enhanced MR imaging data were potentially available for only 79 of the 129 specifically identified nodes. Because of necessary tradeoffs between spatial and time resolution (discussed in more detail below), the dynamic acquisition provided less anatomic coverage than the other sequences and also was acquired with thicker sections. Therefore, a number of nodes for which we had high resolution anatomic imaging and pathologic data either were not included in the dynamic acquisition or were not clearly visible on the dynamic acquisition (mean size of nodes with dynamic contrast-enhanced data, 8.7 mm; mean size of nodes without dynamic contrast-enhanced data, 4.6 mm). Of the 79 potentially evaluable nodes, 11 additional nodes were excluded because of local artifacts (eg, dental amalgam) or patient movement rendering the data uninterpretable, leaving us with 68 nodes for formal analysis. We did have dynamic contrast-enhanced MR imaging data available from every patient, however, with the number of analyzed nodes per patient ranging from two to six.

Signal intensity versus time curves were generated from each node individually. A typical curve is shown in Figure 2, with peak time, peak enhancement, maximum up-slope, and washout slope illustrated. These values were obtained from similar curves for each of the 68 nodes, with anatomic images and representative curves from a tumor-involved and a non-tumor-involved node shown in Figure 3. Tumor-involved nodes had a significantly longer time to peak, lower peak enhancement, and lower maximum slope than did non-tumor-involved nodes (Table 2). They also had a less rapid washout phase compared with non-tumor-involved nodes. Dynamic data were also compiled for easily identifiable normal structures—the submandibular gland and the sternocleidomastoid muscle (Table 3)—and tumor-involved nodes were found to be significantly different from both of these in dynamic contrast enhancement characteristics. The appearance of the sternocleidomastoid muscle curve (in Fig 3) is similar to the muscle uptake curves described by other investigators (27, 28), with a gradual rise and relatively low peak. The submandibular gland had a pattern similar to that of non-tumor-involved nodes, as shown in Figure 3.

A subanalysis of the four nodes with frank necrosis was also performed to determine how the presence of clear-cut necrosis would affect our curves and analysis. Regions of interest were drawn to separately encompass the whole necrotic node versus only the peripheral rim of the necrotic node to assess how the curves varied from each other and whether the curves were significantly different from the average non-tumor curve. This analysis is presented in Table 4 and illustrated in Figure 4. Statistical significance could not be calculated because of the small number of necrotic nodes. Inclusion of the necrotic volume did affect curve magnitudes and absolute values of our calculated parameters; in effect, the necrotic areas scale down the tumor curve by a scaling factor that is a fraction of the necrotic volume, and a more robust curve will be generated if grossly necrotic areas are excluded from the region of interest. We found, however, that although the presence of necrosis altered the absolute values of our calculated parameters, they were still different from normal values. Scaling does not change the shape of the curve and therefore does not change such measurements as peak time.

Discussion

The assessment of the neck for metastatic cervical adenopathy in patients with squamous cell carcinoma of the head and neck is a significant problem in

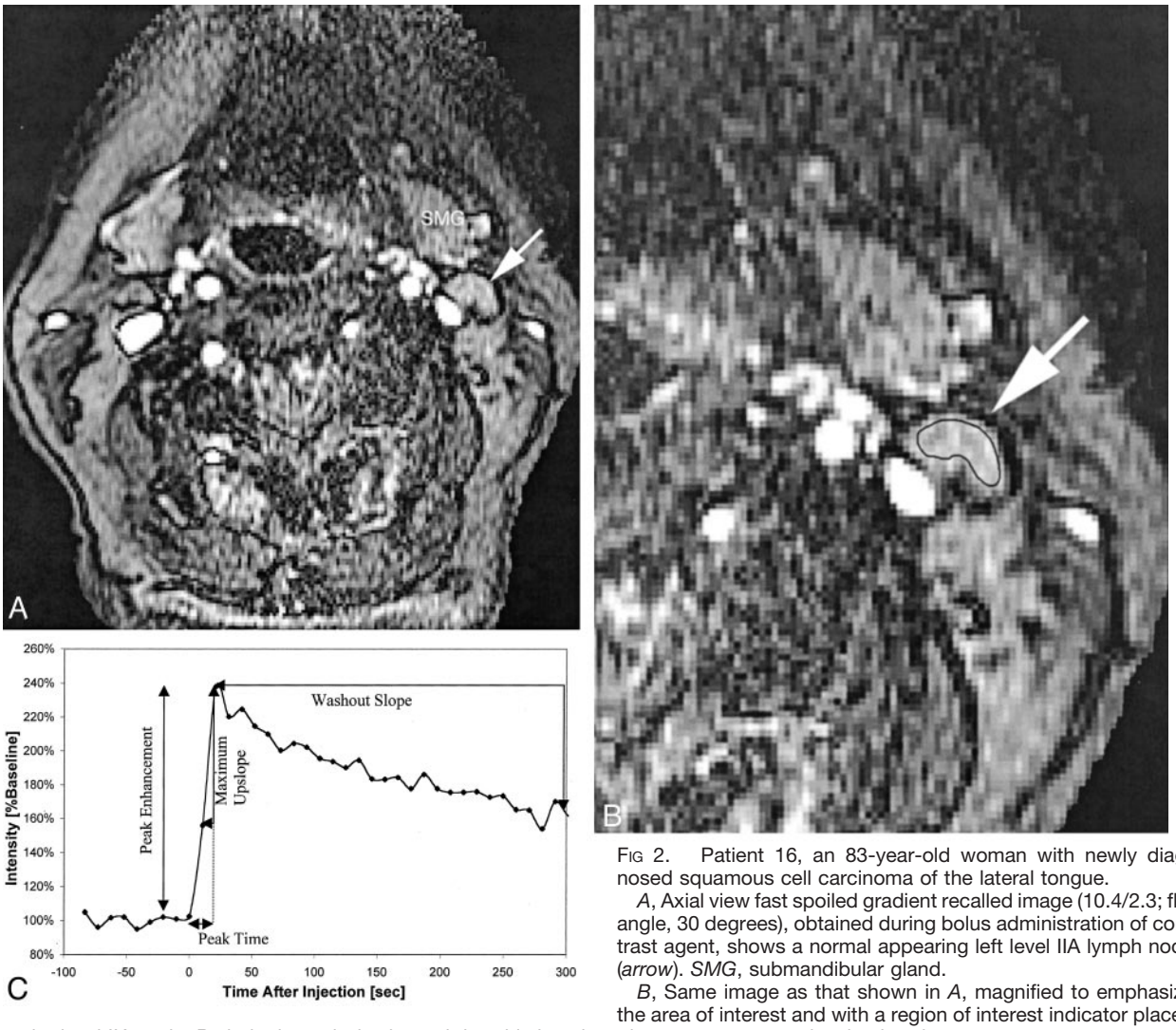

FIG 2. Patient 16, an 83-year-old woman with newly diagnosed squamous cell carcinoma of the lateral tongue.

A, Axial view fast spoiled gradient recalled image (10.4/2.3; flip angle, 30 degrees), obtained during bolus administration of contrast agent, shows a normal appearing left level IIA lymph node (*arrow*). *SMG*, submandibular gland.

B, Same image as that shown in *A*, magnified to emphasize the area of interest and with a region of interest indicator placed over the level IIA node. Pathologic analysis showed that this lymph node was not a tumor-involved node.

C, Plot of signal intensity versus time generated from the region of interest placed around the cervical lymph node shown in *B*. Derivation of peak time, peak enhancement, maximum up-slope, and washout slope are illustrated.

clinical oncology. Limitations in staging by using clinical palpation and conventional anatomic imaging are well known. In 15% to 25% of patients whose necks seem to be N0 based on these methods, nodal metastases will be found at surgery (1, 3–5). Conversely, not all enlarged lymph nodes are tumor-involved nodes; reactive lymphoid hyperplasia is not uncommon in patients with head and neck cancer. Metabolic imaging with ^{18}F-flouorodeoxyglucose positron emission tomography (9) and direct nodal sampling with sonography-guided fine needle aspiration (13) can improve the preoperative assessment, but ^{18}F-flouorodeoxyglucose positron emission tomography is expensive and not widely available, while ultrasonography-fine needle aspiration is not widely practiced outside of a few academic centers. We have shown a potential role for dynamic contrast-enhanced MR imaging in the initial assessment of the patient with head and neck cancer. We hope that further work will support the concept that dynamic contrast-enhanced MR imaging may help to segregate newly diagnosed patients into appropriate treatment categories and may detect early treatment failures when an organ preservation approach is chosen. Although the high resolution anatomic component of imaging is helpful for accurately localizing small nodes, in current practice, it is not sensitive to small foci of tumor in non-necrotic lymph nodes.

High Resolution Anatomic Imaging

Routine anatomic imaging of the neck is usually performed with a section thickness of 3 mm for CT and 4 to 5 mm with a 1- to 2-mm gap for MR imaging. Considerable debate exists regarding whether CT or MR imaging is more effective in showing pathologic lymph nodes (8, 36). Both are effective, and to some extent, the choice may hinge on which technique is chosen to evaluate the primary site. In our practice, most patients with squamous cell carcinoma of the head and neck undergo MR imaging for their initial evaluation and staging. In a 5-mm-thick section with an 18-cm field of view and a 256 × 192 matrix, voxel

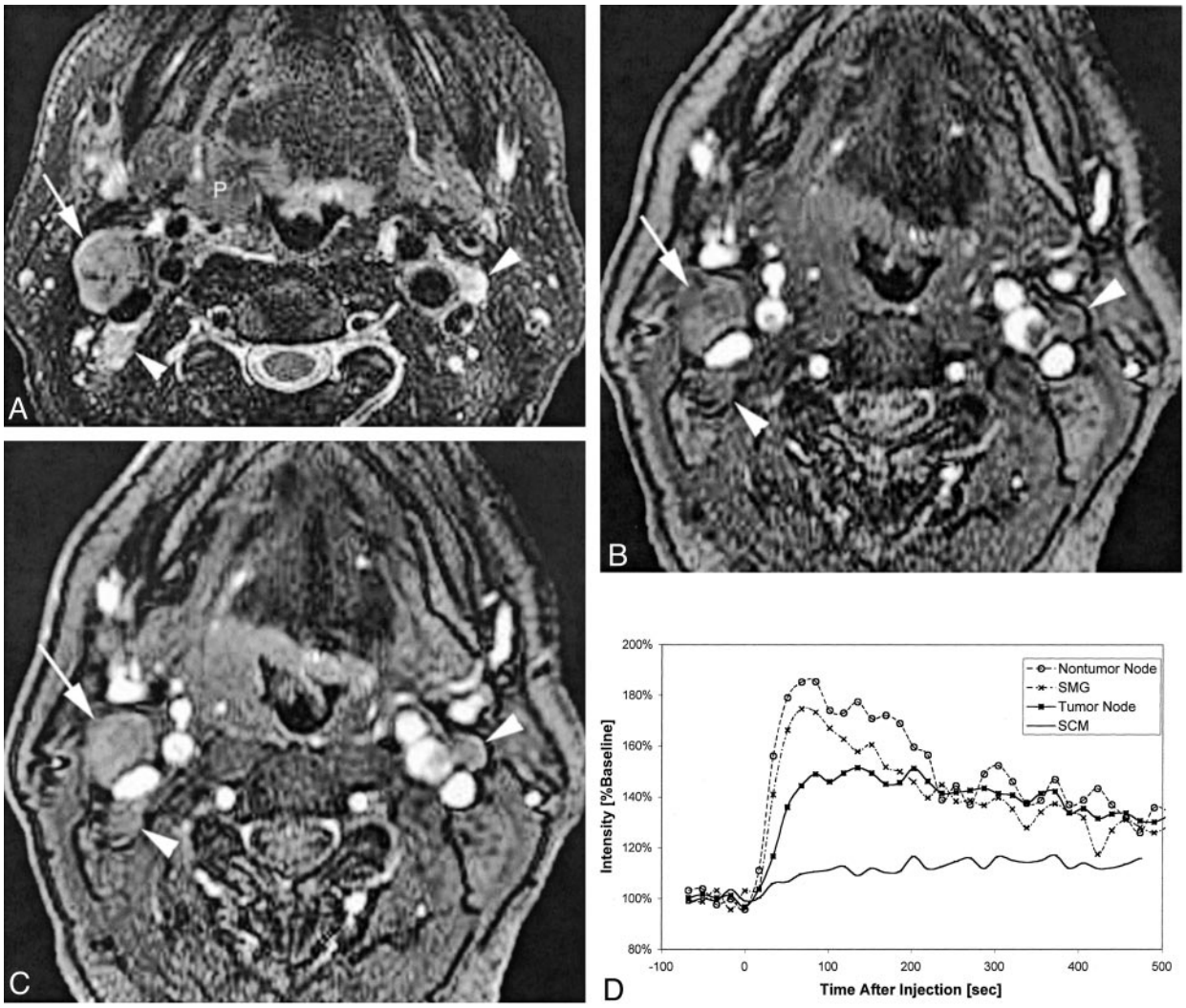

FIG 3. Patient 6, a 57-year-old man with right oropharyngeal cancer and multiple palpable nodes who underwent pharyngectomy, right modified radical neck dissection, and left supraomohyoid neck dissection.

A, Coil-corrected fast spin-echo T2-weighted image with fat saturation (4000/90/4) shows the primary tumor (*P*), a dominant tumor-involved right level IIA node (*white arrow*), and two smaller tumor-involved level IIA lymph nodes (*white arrowheads*) on the right and left sides of the neck.

B, Baseline image (10.4/2.3; flip angle, 30 degrees) from the dynamic sequence shows the same tumor-involved nodes 117 seconds after contrast medium injection.

C, Enhanced dynamic image (10.4/2.3; flip angle, 30 degrees) shows the same tumor-involved nodes.

D, Plot of signal intensity versus time after injection of contrast agent, generated from regions of interest placed on the right level IIA tumor-involved node, a left level III non-tumor-involved node (not included on these images), the submandibular gland (*SMG*), and the sternocleidomastoid muscle (*SCM*). The different curve morphologies generated from these different tissues can be appreciated as shown by this comparison plot.

TABLE 2: Dynamic contrast-enhanced MR imaging features of tumor involved versus non-tumor-involved nodes

	No.	Peak Time (s)	Peak Enhancement (%baseline)	Maximum Slope (%baseline/min)	Washout Slope (%baseline/min)
Tumor-involved	25	111 (68)	176 (30)	193 (123)	−7.6 (5.3)
Non-tumor-involved	43	46 (29)	198 (46)	324 (224)	−12.2 (8.1)
P value		<.001	<.05	<.01	<.05

Note.—Number in parentheses indicates SD. Also note that the washout slope for non-tumor-involved nodes is based on N = 40 rather than 43 because late data points were not acquired for three nodes.

volume will be ($5 \times 0.7 \times 0.94$ mm^3), or 3.3 mm^3. With the high resolution surface coil images, voxel volume is ($2 \times 0.7 \times 0.7$ mm^3), or 1.0 mm^3. Although both CT and MR imaging are sensitive to nodal necrosis, which is considered diagnostic of tumor infiltration, MR imaging is more sensitive to intranodal heterogeneity, which may also be a sign of tumor involvement. It is also possible, however, that a lymph

TABLE 3: Dynamic contrast-enhanced MR imaging characterization of submandibular gland and sternocleidomastoid muscle

Tissue	Peak Time (s)	Peak Enhancement (%baseline)	Maximum Slope (%baseline/min)	Washout Slope (%baseline/min)
SMG	50 (41)	206 (67)	333 (186)	−11.4 (6.6)
SCM	264 (102)	125 (10)	49 (36)	−3.0 (10.9)

Note.—Number in parentheses indicates SD. SMG, submandibular gland; SCM, sternocleidomastoid muscle.

TABLE 4: Subanalysis of whole necrotic node versus peripheral rim only

Tissue	Peak Time (s)	Peak Enhancement (%baseline)	Maximum Slope (%baseline/min)	Washout Slope (%baseline/min)
Whole necrotic node	114 (22)	131 (14)	57 (12)	−0.1 (0.001)
Peripheral rim only	136 (48)	180 (49)	171 (132)	−0.2 (0.05)
Normal node	46 (29)	198 (46)	324 (224)	−12.2 (8.1)

Note.—*P* values cannot be calculated because of the small number of necrotic nodes.

node showing reactive follicular hyperplasia may be somewhat heterogeneous, and answering this question will require more specific pathologic correlation. In two nodes in which internal heterogeneity on high resolution MR images made us suspect that a node was a tumor-involved node, as discussed above, absence of tumor was shown pathologically. Although the high resolution images were very helpful for nodal identification, measurement, and planning for surgical localization, they did not seem to offer a major benefit over good quality conventional imaging in determining the presence or absence of tumor, as assessed by overall neck stage. As discussed under Results, a direct node-to-node comparison of conventional versus high resolution anatomic imaging could not be conducted.

Simple measurement of nodal size has been the focus of much study for identification of tumor involvement of cervical lymph nodes on anatomic images, and much has been written regarding appropriate size criteria for suggesting metastatic involvement (4, 5, 7, 8, 13). In our study, there happened to be a significant difference in mean short axis diameter ($P < .001$) between tumor-involved and non-tumor-involved lymph nodes. There was, however, an overlap between these two groups (with non-tumor-involved nodes as large as 10 mm, and five tumor-involved nodes measuring <10 mm). In addition, some tumor-involved nodes measured as small as 2 to 4 mm when the full neck dissection specimen was assessed, although those nodes were not part of our study because they could not be specifically identified and targeted for selected removal and processing because of their small size. Size criteria are useful in the day-to-day interpretation of imaging studies of patients with head and neck cancer, but their limitations are well known.

Dynamic Contrast-enhanced MR Imaging

Benign as well as malignant lymph nodes show enhancement after the administration of gadolinium-based contrast agents. Tumor microcirculation, however, generally differs from normal tissues in three major ways: the flow characteristics and blood volume of the microvasculature, microvascular permeability, and, for many tumors, an increased fractional volume of the extravascular extracellular space. As has been shown in other parts of the body, including breast, uterine cervix, and bladder (16, 17, 20, 23), we hypothesized that the dynamic component of the signal intensity might be more important than the overall magnitude and that useful diagnostic information could be obtained by monitoring the change in tissue signal intensity induced by a contrast agent over time in cervical lymph nodes. In theory, dynamic contrast-enhanced MR imaging reflects the physiology of the microcirculation, specifically the microvasculature and the extravascular extracellular space because the intracellular space is not accessed by gadolinium-based contrast agents.

Dynamic contrast-enhanced MR imaging has been applied to the head and neck (25–31, 37), but only two studies (29, 37) specifically examined nodal characteristics. Escott et al (25) noted that dynamic gradient-echo MR imaging was superior to conventional contrast-enhanced spin-echo imaging in delineating margins and extent of tumor, but they studied a multitude of pathologic abnormalities and did not analyze signal intensity versus time curves. Others (30, 31) tried to segregate tumor histologies by using patterns of signal intensity curves, achieving limited success. Guckel et al (28) used dynamic contrast-enhanced MR imaging to evaluate signal intensity versus time for 15 patients with squamous cell carcinoma of the oral cavity and oropharynx. They found that the time/intensity curves of the tumors could be divided into two groups, one showing a rapid enhancement pattern with an early peak and then a continuous decrease and one showing a slower but continuous increase that then gradually decreased. No explanation for these differences could be found clinically or histopathologically, and it was hypothesized that differential capillary permeability caused by endothelium defects that would be detectable only by electron microscopy might have been present. Baba et al (27) evaluated the role of dynamic MR imaging in the evaluation of head and neck cancers treated with

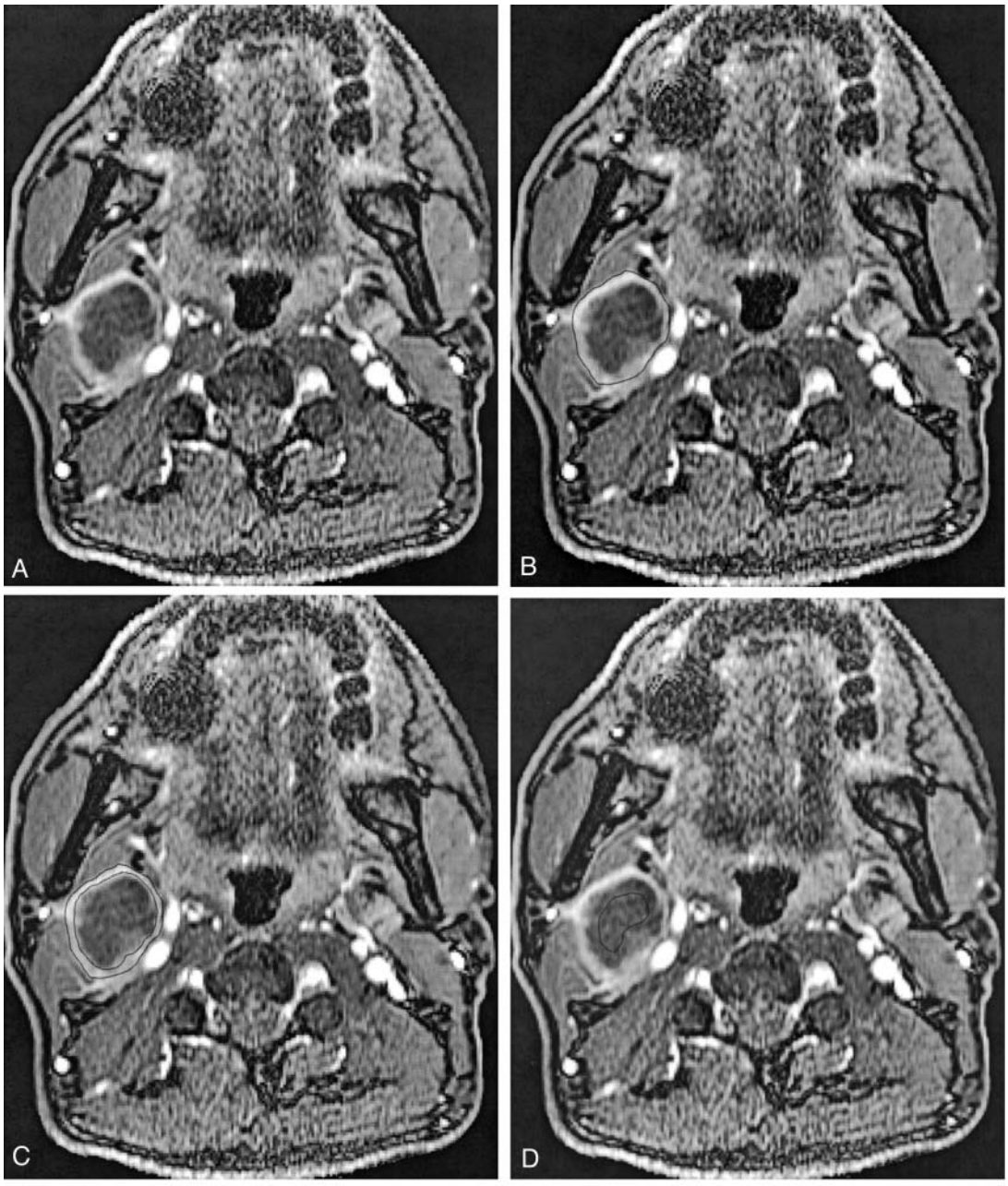

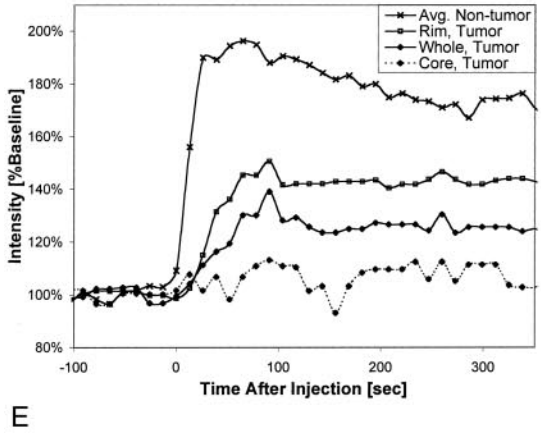

FIG 4. Patient 7, a 52-year-old man who had previously undergone partial glossectomy for squamous cell carcinoma of the tongue, received no additional therapy, and then presented with a palpable right neck mass. Fine needle aspiration confirmed recurrent squamous cell carcinoma in the neck, and MR imaging revealed right cervical necrotic lymphadenopathy. The patient then underwent re-excision of the primary site and a right radical neck dissection.

A, Coil-corrected axial view enhanced dynamic image (10.4/2.3; flip angle, 30 degrees), acquired 195 s into the acquisition, shows a large, centrally necrotic, right level IIA lymph node.

B, Same image as that shown in *A*, with the region of interest encompassing the whole node shown.

C, Same image as that shown in *A*, with the region of interest encompassing only the rim shown.

D, Same image as that shown in *A*, with the region of interest encompassing only the necrotic core shown.

E, Plot of signal intensity versus time from this node, with curves generated from regions of interest placed on the whole node, the rim only, and the necrotic core only. Note that the "rim" curve is very similar to the "whole" curve but appears reduced in magnitude by a scaling factor related to the necrotic core. All these curves appear very different from the average non-tumor curve that is shown for comparison, but a statistically significant comparison was not possible because of the small number of grossly necrotic nodes.

radiation therapy and found that dynamic MR imaging was useful in distinguishing persistent tumor from postradiation fibrosis by showing early enhancement in residual tumor. Section thickness, coverage, and whether nodal tissue as well as primary site tissue had been assessed were not noted. Hoskin et al (29) also assessed dynamic contrast-enhanced MR imaging as a predictor of response to accelerated radiation therapy for advanced head and neck cancer. They found that local control (assessed at a mean of 11.5 months) correlated with a maximum tumor enhancement of <0.8 and a mean fall in time to reach maximum tumor enhancement of 27.3 s. Both primary sites and nodes were included and showed similar results, although curves and regions of interest are not presented. A suggestion was made that the predictive effect of maximum tumor enhancement was greater for primary tumor than for nodes, but no overall differences in calculated parameters between the two subgroups were shown.

Lamer et al (37) studied 14 patients with obvious metastatic adenopathy who were to undergo primary neck dissection. Two-section dynamic MR acquisition was performed and then processed by using factor analysis. In addition, one of the MR sections was directly correlated with a histologic nodal specimen that was stained for microvessel attenuation (microvessel density) analysis. Factor analyses were well defined in only six cases, and two factors could be isolated, with the described enhancement patterns sounding similar to those described by Guckel et al (28) but with an overlap between neoplastic and spared areas. Necrotic areas were not taken into account in this analysis. Microvessel density values of spared lymphoid components and neoplastic tissues showed some overlap, but the mean microvessel density value was higher overall in neoplastic areas (value of 7.6) than in spared areas (value of 3.64).

In other areas of the body (16, 17, 20, 23), dynamic contrast analysis has focused mainly on primary tumor sites. A recent article by Kvistad et al (24), however, assessed the role of dynamic contrast-enhanced MR imaging in the preoperative detection of axillary lymph node metastases in breast cancer. The authors found that if a signal intensity increase of >100% during the first contrast-enhanced imaging session was used as a threshold for malignancy, then 57 of 65 patients were correctly classified. Limitations of the study included lack of effort to make direct comparison between specific lymph nodes detected by MR imaging and by histopathology, and the classification of lymph nodes that were too small to allow definite region of interest measurement on the dynamic contrast-enhanced MR images as normal. Necrosis was not specifically accounted for in the region of interest analysis.

For our patients, we looked specifically at the cervical lymph nodes. We found that time to peak enhancement was longer and that both peak enhancement and maximum slope of wash in of contrast agent were lower in tumor-involved compared with non-tumor-involved lymph nodes. The washout phase was also less rapid for tumor-involved nodes as compared with non-tumor-involved nodes. These results were somewhat different from what we had expected. We had hypothesized that the disorganized, permeable neovessels associated with malignancy would result in a more rapid and more intense peak during wash in of contrast agent that would rise with a steeper slope than that of normal tissues (14, 38). Lymphoid tissue does, however, have higher blood flow than squamous cell carcinoma of the head and neck (39), which may explain this result, at least in part. Our data indicated that tumor tissue actually has lower transfer of contrast agent to tissue (a function of blood flow, blood volume, and vessel permeability, thus lower time to peak and lower maximum up-slope) and that tumor tissue has a decreased volume of extravascular, extracellular space (hence lower peak enhancement) compared with normal or reactive nodal tissue. Although neovessels are thought to be more permeable than normal vessels, this enhanced permeability has been shown for macromolecules and does not necessarily apply to a 500-Da molecule such as gadolinium diethylenetriamine penta-acetic acid in the absence of the blood-brain barrier (14, 38). Furthermore, tumor tissue does not necessarily have increased blood flow and volume compared with normal lymphoid tissue, especially if the nodal tissue is reactive. Tumor blood flow is known to be heterogeneous, slow, and even retrograde (39, 40). Additionally, there are conflicting reports regarding whether microvessel density is definitely increased in squamous cell carcinoma of the head and neck, so blood volume cannot be assumed to be increased. Furthermore, because this was not a first-pass study, blood volume and permeability information cannot be reliably extracted in an individual manner. Another potential issue is the enhanced interstitial fluid pressure in tumors, a situation that is thought to represent a major obstacle to delivery of therapeutic agents (41, 42) and may impede the transfer of contrast agent to extravascular tissue. Finally, we do not know the extent to which we are volume averaging solid masses of neoplastic cells and foci of "micronecrosis" (ie, areas of necrosis that are below our resolution on even high resolution anatomic images), and this could also influence our results. Considering that we were dealing with squamous cell carcinomas, it is also possible that areas of desquamated keratin ("keratin pools") might have influenced the transfer of contrast agent to tissues and hence our results. A hope for the future is to obtain more detailed histopathologic analysis of sampled nodes to directly investigate microvessel density and the presence of areas of micronecrosis or keratin pooling.

The region of interest analysis method, although ingrained in the dynamic contrast-enhanced MR imaging literature, is also potentially problematic. The drawing of a region of interest around an often small and irregularly shaped structure, such as a lymph node, is subject to error and may result in inclusion of non-nodal tissue in the region of interest. Furthermore, the simple extraction of a mean pixel value may

offer only a limited view of nodal composition, particularly if there is significant tissue heterogeneity (on a macro- or microscopic level) (40). Liney et al (19) addressed this issue in reference to breast tumors, retrospectively evaluating three distinct methods of region of interest selection. Each method returned differing values, showing that further work in this area is clearly needed. Improved spatial resolution to improve region of interest drawing combined with automated methods to improve reproducibility will be important components of future studies based on region of interest analysis.

We have reported results that depend to some extent on our chosen sequence parameters and do not provide direct information regarding physiological parameters such as the volume transfer constant or the volume of the extravascular extracellular space per unit volume of tissue (38). With dynamic contrast-enhanced MR imaging, only change in signal intensity amplitude is measured, and this may not be easily related to the concentration of contrast agent in the tissue (40). A variety of models have been developed to allow estimation of kinetic parameters from dynamic contrast-enhanced MR imaging of a diffusible tracer such as gadopentetate dimeglumine (38). Standardization of acquisition parameters and the development of algorithms to automatically extract arterial input functions from dynamic contrast-enhanced MR imaging data will allow reproducible assessment of contrast agent uptake rates (43). We compared tumor-involved and non-tumor-involved nodes within in the same person to avoid blood clearance issues and assumptions, but this does not accomplish prospective identification of tumor-involved versus non-tumor-involved nodes because it still relies on relative rather than absolute characterizations. Although the acquisition and description of heuristic parameters may provide useful information, the application of pharmacokinetic modeling has the potential to standardize results and provide true quantification of physiological parameters. As more groups generate data from dynamic contrast-enhanced MR imaging, actual physiological parameters that can be compared among groups will be essential to understanding these processes on a tissue level.

Many avenues are available for future study of cervical lymph nodes in patients with squamous cell carcinoma of the head and neck with the use of dynamic contrast-enhanced MR imaging techniques. As MR gradients improve, temporal and spatial resolution should also improve, allowing us to obtain thinner sections with more time points and greater anatomic coverage when using dynamic acquisition. Alternatively, along the line of the "sentinel node" theory (44, 45), it may be possible to direct dynamic contrast-enhanced MR imaging to a node or nodes of a certain position (based on the site and size of the primary tumor) rather than having to screen the entire neck to obtain potentially useful information for patients whose necks are clinically staged as N0. The ability to accurately assess an arterial input function by using MR imaging will allow calculation of physiological parameters. Additionally, more specific pathologic correlation will allow us to assess the influence of specific histologic features on dynamic contrast-enhanced MR images. Finally, in our case, as with others using gadopentetate dimeglumine for dynamic contrast-enhanced MR imaging, we are potentially dealing with a situation in which capillary permeability is so high that the system is flow limited and in which separation of the intravascular and extravascular extracellular compartments is not possible. The development of safe macromolecular contrast agents will allow assessment of blood flow and volume in areas of the body in which a blood-tissue barrier does not exist.

Conclusion

We have used dynamic contrast-enhanced MR imaging to assess cervical lymph nodes in patients with squamous cell carcinoma of the head and neck. Tumor-involved lymph nodes behave differently from non-tumor-involved nodes on dynamic contrast-enhanced MR images. They have a longer time to peak, reduced peak enhancement, reduced maximum slope, and slower washout slope. Our data are consistent with decreased transfer of contrast agent to tissue and reduced volume of the extravascular extracellular space in tumor-involved nodes as compared with normal or reactive lymph nodes. Although at present, anatomic imaging is the primary method for nodal staging, it is limited by trade-offs between sensitivity and specificity inherent in size criteria and the relative infrequency of nodal necrosis. Metabolic methods (^{18}F-flouorodeoxyglucose positron emission tomography, superparamagnetic iron oxide lymphography) are costly and not widely available, whereas ultrasound-guided fine needle aspiration is very labor intensive and not widely practiced. The dynamic contrast-enhanced technique can be performed as a fairly simple add-on to routine MR imaging and may provide additional useful physiological information regarding nodal staging in patients with squamous cell carcinoma of the head and neck.

Acknowledgment

We appreciate the helpful comments of Tim Roberts, PhD.

References

1. Hao SP, Ng SH. **Magnetic resonance imaging versus clinical palpation in evaluating cervical metastasis from head and neck cancer.** *Otolaryngol Head Neck Surg* 2000;123:324–327
2. Kau RJ, Alexiou C, Stimmer H, Arnold W. **Diagnostic procedures for detection of lymph node metastases in cancer of the larynx.** *ORL J Otorhinolaryngol Relat Spec* 2000;62:199–203
3. van den Brekel MW, Castelijns JA, Croll GA, et al. **Magnetic resonance imaging vs palpation of cervical lymph node metastasis.** *Arch Otolaryngol Head Neck Surg* 1991;117:663–673
4. Som PM. **Lymph nodes of the neck.** *Radiology* 1987;165:593–600
5. van den Brekel MW, Stel HV, Castelijns JA, et al. **Cervical lymph node metastasis: assessment of radiologic criteria.** *Radiology* 1990; 177:379–384
6. Yousem DM, Som PM, Hackney DB, Schwaibold F, Hendrix RA. **Central nodal necrosis and extracapsular neoplastic spread in**

cervical lymph nodes: MR imaging versus CT. *Radiology* 1992;182: 753–759
7. van den Brekel MW, Castelijns JA, Stel HV, et al. **Detection and characterization of metastatic cervical adenopathy by MR imaging: comparison of different MR techniques.** *J Comput Assist Tomogr* 1990;14:581–589
8. Curtin HD, Ishwaran H, Mancuso AA, Dalley RW, Caudry DJ, McNeil BJ. **Comparison of CT and MR imaging in staging of neck metastases.** *Radiology* 1998;207:123–130
9. Benchaou M, Lehmann W, Slosman DO, et al. **The role of FDG-PET in the preoperative assessment of N-staging in head and neck cancer.** *Acta Otolaryngol* 1996;116:332–335
10. Anzai Y, Prince MR. **Iron oxide-enhanced MR lymphography: the evaluation of cervical lymph node metastases in head and neck cancer.** *J Magn Reson Imaging* 1997;7:75–81
11. Tschammler A, Ott G, Schang T, Seelbach-Goebel B, Schwager K, Hahn D. **Lymphadenopathy: differentiation of benign from malignant disease: color Doppler US assessment of intranodal angioarchitecture.** *Radiology* 1998;208:117–123
12. Moritz JD, Ludwig A, Oestmann JW. **Contrast-enhanced color Doppler sonography for evaluation of enlarged cervical lymph nodes in head and neck tumors.** *AJR Am J Roentgenol* 2000;174: 1279–1284
13. van den Brekel MW, Castelijns JA, Stel HV, et al. **Occult metastatic neck disease: detection with US and US-guided fine-needle aspiration cytology.** *Radiology* 1991;180:457–461
14. Parker GJ, Tofts PS. **Pharmacokinetic analysis of neoplasms using contrast-enhanced dynamic magnetic resonance imaging.** *Top Magn Reson Imaging* 1999;10:130–142
15. Roberts HC, Roberts TP, Brasch RC, Dillon WP. **Quantitative measurement of microvascular permeability in human brain tumors achieved using dynamic contrast-enhanced MR imaging: correlation with histologic grade.** *AJNR Am J Neuroradiol* 2000;21: 891–899
16. den Boer JA, Hoenderop RK, Smink J, et al. **Pharmacokinetic analysis of Gd-DTPA enhancement in dynamic three-dimensional MRI of breast lesions.** *J Magn Reson Imaging* 1997;7:702–715
17. Heiberg EV, Perman WH, Herrmann VM, Janney CG. **Dynamic sequential 3D gadolinium-enhanced MRI of the whole breast.** *Magn Reson Imaging* 1996;14:337–348
18. Knopp MV, Weiss E, Sinn HP, et al. **Pathophysiologic basis of contrast enhancement in breast tumors.** *J Magn Reson Imaging* 1999;10:260–266
19. Liney GP, Gibbs P, Hayes C, Leach MO, Turnbull LW. **Dynamic contrast-enhanced MRI in the differentiation of breast tumors: user-defined versus semi-automated region-of-interest analysis.** *J Magn Reson Imaging* 1999;10:945–949
20. Hawighorst H, Knapstein PG, Weikel W, et al. **Cervical carcinoma: comparison of standard and pharmacokinetic MR imaging.** *Radiology* 1996;201:531–539
21. Mayr NA, Hawighorst H, Yuh WT, Essig M, Magnotta VA, Knopp MV. **MR microcirculation assessment in cervical cancer: correlations with histomorphological tumor markers and clinical outcome.** *J Magn Reson Imaging* 1999;10:267–276
22. Lang P, Honda G, Roberts T, et al. **Musculoskeletal neoplasm: perineoplastic edema versus tumor on dynamic postcontrast MR images with spatial mapping of instantaneous enhancement rates.** *Radiology* 1995;197:831–839
23. Barentsz JO, Engelbrecht M, Jager GJ, et al. **Fast dynamic gadolinium-enhanced MR imaging of urinary bladder and prostate cancer.** *J Magn Reson Imaging* 1999;10:295–304
24. Kvistad KA, Rydland J, Smethurst HB, Lundgren S, Fjosne HE, Haraldseth O. **Axillary lymph node metastases in breast cancer: preoperative detection with dynamic contrast-enhanced MRI.** *Eur Radiol* 2000;10:1464–1471
25. Escott EJ, Rao VM, Ko WD, Guitierrez JE. **Comparison of dynamic contrast-enhanced gradient-echo and spin-echo sequences in MR of head and neck neoplasms.** *AJNR Am J Neuroradiol* 1997;18:1411–1419
26. Baba Y, Yamashita Y, Onomichi M, Murakami R, Takahashi M. **Dynamic magnetic resonance imaging of head and neck lesions.** *Top Magn Reson Imaging* 1999;10:125–129
27. Baba Y, Furusawa M, Murakami R, et al. **Role of dynamic MRI in the evaluation of head and neck cancers treated with radiation therapy.** *Int J Radiat Oncol Biol Phys* 1997;37:783–787
28. Guckel C, Schnabel K, Deimling M, Steinbrich W. **Dynamic snapshot gradient-echo imaging of head and neck malignancies: time dependency and quality of contrast-to-noise ratio.** *MAGMA* 1996; 4:61–69
29. Hoskin PJ, Saunders MI, Goodchild K, Powell ME, Taylor NJ, Baddeley H. **Dynamic contrast enhanced magnetic resonance scanning as a predictor of response to accelerated radiotherapy for advanced head and neck cancer.** *Br J Radiol* 1999;72:1093–1098
30. Takashima S, Noguchi Y, Okumura T, Aruga H, Kobayashi T. **Dynamic MR imaging in the head and neck.** *Radiology* 1993;189: 813–821
31. Zagdanski AM, Sigal R, Bosq J, Bazin JP, Vanel D, Di Paola R. **Factor analysis of medical image sequences in MR of head and neck tumors.** *AJNR Am J Neuroradiol* 1994;15:1359–1368
32. Henry RG, Fischbein NJ, Dillon WP, Vigneron DB, Nelson SJ. **High-sensitivity coil array for head and neck imaging: technical note.** *AJNR Am J Neuroradiol* 2001;22:1881–1886
33. Lindberg R. **Distribution of cervical lymph node metastases from squamous cell carcinoma of the upper respiratory and digestive tracts.** *Cancer* 1972;29:1446–1449
34. Wald LL, Carvajal L, Moyher SE, et al. **Phased array detectors and an automated intensity correction algorithm for high resolution MR imaging of the human brain.** *Magn Reson Med* 1995;34:433–439
35. Nakayama E, Ariji E, Shinohara M, Yoshiura K, Miwa K, Kanda S. **Computed tomography appearance of marked keratinization of metastatic cervical lymph nodes: a case report.** *Oral Surg Oral Med Oral Pathol Oral Radiol Endod* 1997;84:321–326
36. van den Brekel MW. **Lymph node metastases: CT and MRI.** *Eur J Radiol* 2000;33:230–238
37. Lamer S, Sigal R, Lassau N, et al. **Radiologic assessment of intranodal vascularity in head and neck squamous cell carcinoma: correlation with histologic vascular density.** *Invest Radiol* 1996;31: 673–679
38. Tofts PS, Brix G, Buckley DL, et al. **Estimating kinetic parameters from dynamic contrast-enhanced T(1)-weighted MRI of a diffusable tracer: standardized quantities and symbols.** *J Magn Reson Imaging* 1999;10:223–232
39. Vaupel P. **Tumor blood flow.** In: Molls M, Vaupel P, eds. *Blood Perfusion and Microenvironment of Human Tumors.* Berlin: Springer-Verlag; 1998:43
40. Evelhoch JL. **Key factors in the acquisition of contrast kinetic data for oncology.** *J Magn Resom Imaging* 1999;10:254–259
41. Milosevic MF, Fyles AW, Hill RP. **The relationship between elevated interstitial fluid pressure and blood flow in tumors: a bioengineering analysis.** *Int J Radiat Oncol Biol Phys* 1999;43:1111–1123
42. Rutz HP. **A biophysical basis of enhanced interstitial fluid pressure in tumors.** *Med Hypotheses* 1999;53:526–529
43. Rijpkema M, Kaanders JH, Joosten FB, van der Kogel AJ, Heerschap A. **Method for quantitative mapping of dynamic MRI contrast agent uptake in human tumors.** *J Magn Reson Imaging* 2001; 14:457–463
44. Mozzillo N, Chiesa F, Botti G, et al. **Sentinel node biopsy in head and neck cancer.** *Ann Surg Oncol* 2001;8[suppl 9]:103S–105S.
45. Taylor RJ, Wahl RL, Sharma PK, et al. **Sentinel node localization in oral cavity and oropharynx squamous cell cancer.** *Arch Otolaryngol Head Neck Surg* 2001;127:970–974